A Temporal Model of Cofilin Regulation and the Early Peak of Actin Barbed Ends in Invasive Tumor Cells

Nessy Tania,[†] Erin Prosk,[†] John Condeelis,[‡] and Leah Edelstein-Keshet[†*]
[†]Department of Mathematics, University of British Columbia, Vancouver, British Columbia, Canada; and [‡]Department of Anatomy and Structural Biology, Gruss Lipper Biophotonics Center, Albert Einstein College of Medicine of Yeshiva University, Bronx, New York

ABSTRACT Cofilin is an important regulator of actin polymerization, cell migration, and chemotaxis. Recent experimental data on mammary carcinoma cells reveal that stimulation by epidermal growth factor (EGF) generates a pool of active cofilin that results in a peak of actin filament barbed ends on the timescale of 1 min. Here, we present results of a mathematical model for the dynamics of cofilin and its transition between several pools in response to EGF stimulation. We describe the interactions of phospholipase C, membrane lipids (PIP_2), and cofilin bound to PIP_2 and to F-actin, as well as diffusible cofilin in active G-actin-monomer-bound or phosphorylated states. We consider a simplified representation in which the thin cell edge (lamellipod) and the cell interior are represented by two compartments that are linked by diffusion. We demonstrate that a high basal level of active cofilin stored by binding to PIP_2, as well as the highly enriched local milieu of F-actin at the cell edge, is essential to capture the EGF-induced barbed-end amplification observed experimentally.

INTRODUCTION

Eukaryotic cell motility relies on polymerization of F-actin to generate protrusive forces at the leading edge of the cell. This polymerization requires available fast-growing barbed ends for actin monomer addition. Indeed, in response to stimulation by epidermal growth factor (EGF), a large peak of barbed ends is observed to form in mammary carcinoma cells ~1 min poststimulus. This peak has been found to be cofilin-dependent (1). Local activation of cofilin has been shown to lead to protrusion initiation and to determine the cell direction (1,2). Further, suppression of cofilin (via knockdown) in the same tumor cell type leads to cells with decreased protrusion velocity and chemotaxis (3,4).

Nucleation of new barbed ends by Arp2/3 is well known, but a similar role for cofilin has recently become apparent (5). Cofilin plays multiple roles, depending on conditions. These include disassembly and/or debranching of the actin dendritic network, as well as de novo F-actin nucleation (6–9). Here, we are concerned only with the role of cofilin in generating the first peak of barbed ends created downstream of EGF stimulation (10).

Cofilin has several states inside the cell. It can bind to F- or G-actin (preferring ADP- rather than ATP-actin (7,11)); it has freely diffusing dephosphorylated (active) and phosphorylated (inactive) forms (12,13). In resting carcinoma cells, van Rheenen et al. (14) found that there is a pool of cofilin bound to the phosphoinositide phosphatidylinositol 4,5-bisphosphate (PIP_2), and hence inactive (15), at the cell membrane.

Although both phosphorylated and dephosphorylated cofilin can bind to PIP_2 (16), only dephosphorylated cofilin was found to be enriched in the plasma membrane (17). Upon EGF stimulation, phospholipase-C (PLC) is activated and hydrolyzes PIP_2 (into inositol trisphosphate and diacylglycerol), so that PIP_2 falls to 40–60% of its basal level (1,14). Active cofilin (no longer taken up as rapidly by PIP_2) becomes available in the cytoplasmic region adjoining the membrane. Our hypothesis is that this effective flux, together with the high local density of cytoskeleton leads to the rapid barbed-end peak. After severing F-actin, cofilin carries an actin monomer and has to be recharged. Phosphorylation by LIM kinase (LIMK) releases cofilin's bound G-actin, and dephosphorylation by slingshot phosphatase (SSH) allows cofilin to rebind to PIP_2, completing its cycle.

It has been suggested that a single cofilin protein can interact with one or more PIP_2 molecules (18). Thus, the twofold PIP_2 drop would be consistent with a similar drop of PIP_2-cofilin or a twofold increase of active cofilin. And yet, the peak of barbed ends is 10- to 15-fold higher than its basal level. This leads to our main question of what creates the observed barbed-end amplification. In addition, we address the following questions:

1. Can cofilin dynamics alone account for the large transient pulse of actin filament barbed ends observed within 1 min of EGF stimulation of carcinoma cells? How does this amplification occur?
2. Based on experimental observations, what are the flows of cofilin between the various pools described above?
3. How much cofilin is in the freely diffusing active form in the resting versus stimulated cell?
4. What are the effects of overexpressing or inhibiting the various agents that control the flows of cofilin between compartments?

Submitted November 2, 2010, and accepted for publication February 22, 2011.

*Correspondence: keshet@math.ubc.ca

Editor: Andre Levchenko.

© 2011 by the Biophysical Society

0006-3495/11/04/1883/10 $2.00

doi: 10.1016/j.bpj.2011.02.036

To quantify the dynamics and compare with experimental data, we assembled several mathematical models, as described below.

MATHEMATICAL MODELS

Barbed-end amplification

Our preliminary model addresses the large barbed-end amplification. From here on, we define amplification as the ratio of barbed-end peak amplitude to barbed-end steady-state level in the resting state (B_{peak}/B_{ss}). Large amplification implies a low basal level of severing and/or a large peak after stimulus. The rapid growth of barbed ends could result from 1), de novo actin nucleation; 2), Arp2/3 mediated branching; or 3), severing of the filaments. Of these possible causes, we rejected the first, since spontaneous nucleation of filaments is slow (19) and limited by profilin (20). As for the second, experiments with PLC inhibitors and cofilin siRNA rule out Arp2/3 in the first peak of barbed ends, and demonstrate its involvement in a later second peak (1). This left the third hypothesis, which is explored further below.

We considered an elementary model for active cofilin (C) and barbed ends (B), with basal rates of production (I_B, I_C); cofilin inactivation, k_p; and barbed-end capping, k_{cap}:

$$\frac{dC}{dt} = \bar{I}_{stim}(t) + I_C - k_p C - F_{sev}(C), \quad (1)$$

$$\frac{dB}{dt} = I_B - k_{cap} B + \bar{A} F_{sev}(C). \quad (2)$$

($\bar{A}$ converts units of C (μM) to units of B (number/μm^2).) We assumed that $\bar{I}_{stim}(t) = 0$ before stimulation, so there is very little severing activity. Poststimulus, $\bar{I}_{stim}(t) = I_0 > 0$, and barbed ends are generated by severing F-actin.

Nonlinear kinetics of severing

We asked what type of severing kinetics, $F_{sev}(C)$, could account for the observed high amplification for $B(t)$ and explored three possibilities: 1), a linear function, 2), a saturating function, and 3), a Hill function far from saturation. Analysis of Eqs. 1 and 2, shown in the Supporting Material, reveals that the cofilin dependence of the first barbed-end peak requires severing kinetics to be nonlinear and operating far from saturation, i.e., the third possibility. We ascribe this nonlinearity to the cooperative nature of cofilin binding to F-actin (21,22). This preliminary exploration informed our choice of the function $F_{sev}(C)$ in Eq. 2.

$$F_{sev}(C) = k_{sev}\, C_{rest} \left(\frac{C}{C_{rest}}\right)^n, \quad (3)$$

where C_{rest} is the concentration of cofilin in the resting state, n the degree of cooperativity (21), and k_{sev} a constant. Note that the form of Eq. 3 is equivalent to a Hill function commonly used in cooperative kinetics, but in a regime far from saturation.

We asked whether the possible rounds of severing, F-actin polymerization, further severing, etc., could also account for a similar autocatalytic effect. We rejected this possibility for several reasons. First, total F-actin only doubles on the timescale of interest (23), far short of the observed factor of 10. Second, unlike Arp2/3, cofilin preferentially binds to ADP or ADP-P_i-F-actin (5). This would lead to some delay in a further round of severing while filaments lose their phosphate groups. Third, as older filaments recede from the cell edge, they are bound by tropomyosin and protected from further severing by cofilin (23). This limits the ability of self-amplification due to autocatalytic growth, leading us to reject such alternatives.

Cofilin regulation model

We now turn to more detailed models for the cofilin cycle in mammary carcinoma cells (1,14,17). We consider only the events leading up to the first peak of barbed ends post-EGF stimulation, constraining the model to match both basal levels of all intermediates (before stimulation) and the transient after the stimulus. Well-measured intermediates such as PLC and PIP_2 are used as inputs, and the size, timing, and shape of the peak of barbed ends are used to appraise the model's predictive ability. The model also predicts cofilin flows between the various pools, both those observed experimentally, and those that are below experimental resolution.

A first attempt to model the cofilin cycle within a single spatial compartment failed to account for certain observations (see the Supporting Material). Here, we present the two-compartment model shown schematically in Fig. 1 (see the Supporting Material for the original and the Appendix for scaled-model equations). The compartments correspond to a small region (~200 nm in width (23)) of cell edge adjacent to the membrane, and the cell interior with volumes V_E and V_I (see Fig. 1 enlarged in the Supporting Material). A small cylindrical surface of height l forms the interface between these volumes, through which diffusion can take place, as explained in the Supporting Material. Activation of PLC (denoted $PLC(t)$) downstream of the EGF signal leads to hydrolysis of PIP_2 ($P_2(t)$). We track five cofilin forms: cofilin bound to F-actin ($C_f(t)$) and to PIP_2 on the membrane ($C_2(t)$), both resident at the cell edge; and diffusible forms of cofilin, i.e., active ($C_a(t)$), actin-monomer-bound ($C_m(t)$), and inactive/phosphorylated ($C_p(t)$) cofilin, which can exchange between compartments. C_i^E and C_i^I denote diffusible cofilin concentrations in the edge/interior compartments. Basic assumptions include

Conservation. On the timescale of interest (a few minutes), synthesis/degradation of cofilin is negligible, and the total amount of cofilin is roughly conserved. Thus,

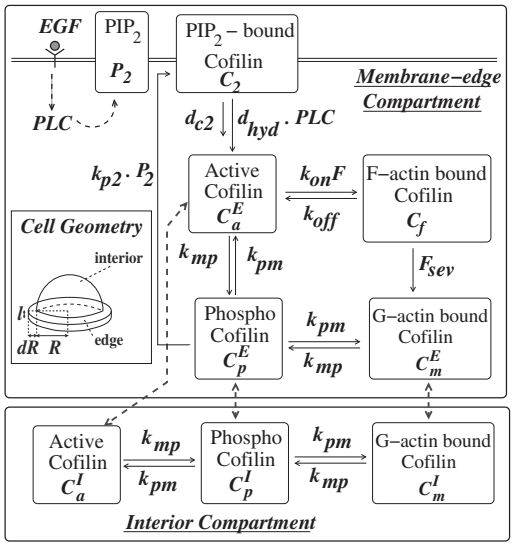

FIGURE 1 Schematics of the cell geometry and the cofilin regulation pathway used in the model. Cell geometry (also see Supporting Material for enlarged view): interior compartment (volume V_I) is approximated as a hemisphere of radius $R \approx$ 5–10 μm. Edge compartment (volume V_E) is shaped like a thin, flat washer (width dR, thickness l, both ~200 nm) (14,24). Note that the figure is not to scale, as $dR << R$. Schematics of the cofilin regulation pathway of the ordinary-differential-equation model. The PIP_2-bound cofilin, C_2, and the F-actin-bound form, C_f, are restricted to the membrane edge compartment, whereas the other forms can diffuse between the two compartments (*gray dashed arrows*). Other arrows in the figure represent reaction terms in the equations (see Appendix and Supporting Material).

$$V_E\left(C_2 + C_a^E + C_f + C_m^E + C_p^E\right) + V_I\left(C_a^I + C_m^I + C_p^I\right) = (V_E + V_I)C_{tot}, \quad (4)$$

where C_{tot}, the whole-cell total cofilin concentration, is assumed constant.

Severing due to F-actin bound cofilin. We assume that cofilin must be bound to F-actin (C_F) to sever it. We adopt $F_{sev} = F_{sev}(C_f)$ from Eq. 3.

PIP_2 hydrolysis. The basal PIP_2 hydrolysis rate was based on PIP_2 FRET (14): post-EGF stimulus, PIP_2 drops by 40–60%, then recovers to 80% of baseline within 360 s (14). From this, we estimated the recovery rate at $d_{p2} = \log 2/360 \sim 0.002$/s.

Binding and unbinding to F-actin. We based the unbinding rate, $k_{off} = 0.005$/s, on in vitro data (7). We assume that F-actin binding sites for cofilin are not limiting, so that $k_{on}F$ is approximately the constant representing the on-rate of cofilin binding to actin.

Phosphorylation and dephosphorylation. We first consider the case where rates of both phosphorylation (k_{mp}) and dephosphorylation (k_{pm}) are constant and similar for the two forms of cofilin, C_a, and C_m.

Actin monomer binding. Although the transition between C_p and C_m is a two-step process, we assume that it is only limited by the phosphorylation and dephosphorylation rates. As a simplification, G-actin binding/unbinding is assumed to be instantaneous and not limited by actin monomer availability. (This is reasonable in view of the ample level of actin monomers in cells, but see (24).)

Rebinding to PIP_2. We assumed that poststimulus recovery of C_2 follows rebinding of phosphocofilin to PIP_2, making the conversion $C_p^E \rightarrow C_2$ (rate k_{p2}).

Flux between compartments. Because compartments are of vastly different sizes, our balance equations contain compartment volume factors to preserve mass conservation (Appendix and Supporting Material). We assume that the cofilin flux between compartments is diffusive, and thus proportional to concentration gradients.

To compare model predictions with experimental observations, we also quantify barbed ends, $B(t)$, using Eq. 2 as before, with $F_{sev} = F_{sev}(C_F)$, and $I_B = 0$.

Scaling and parameter determination

Because most experimental results quantify levels of variables relative to their basal level, we scale the model accordingly. PLC, P_2, and B are divided by their unstimulated steady-state values, and the cofilin forms by the total mean cofilin concentration in the cell, C_{tot}. Original variables are denoted in capital letters, and the corresponding scaled variables in lower-case letters (see Appendix), so that c_j^E, c_j^I are, respectively, the edge and interior scaled concentrations of cofilin form j. We also define the compartment volume fractions $v_E = V_E/(V_E + V_I)$ and $v_I = V_I/(V_E + V_I)$, so that the conservation statement (Eq. 4) becomes

$$v_E\left(c_2 + c_a^E + c_f + c_m^E + c_p^E\right) + v_I\left(c_a^I + c_m^I + c_p^I\right) = 1, \quad (5)$$

The total whole-cell fraction of cofilin in form j is then given by $v_E\, c_j^E + v_I\, c_j^I$. We further denote the steady-state fractions as

$$R_2 \equiv \frac{V_E}{V_E + V_I}\frac{C_2}{C_{tot}} = v_E c_2,\ R_f \equiv \frac{V_E}{V_E + V_I}\frac{C_F}{C_{tot}} = v_E c_f, \quad (6)$$

$$R_a \equiv v_E c_a^E + v_I c_a^I,\ R_p \equiv v_E c_p^E + v_I c_p^I,\ R_m \equiv v_E c_m^E + v_I c_m^I.$$

Equations 5 and 6 then imply that $R_2 + R_a + R_m + R_P + R_f = 1$. Song et al. (17) found the fraction of phosphorylated cofilin before EGF stimulation (R_p) to be 20%. Van Rheenen et al. (14) observed that most of the cofilin residing at the edge is bound to either F-actin or to PIP_2. They further showed that the ratio between the PIP_2- and the F-actin-bound cofilin is 85%:15%, so we similarly take $R_2/R_f = 0.85/0.15$. The fraction of PIP_2-bound cofilin, R_2, has not been determined experimentally. A lower estimate of 10%

has been measured (R. Eddy and J. Condeelis, unpublished). The fraction of diffusible active cofilin, R_a, is difficult to measure experimentally. We used data fitting to quantify both R_a and R_2. Finally, R_m can be determined from the conservation condition.

Parameter values (Table 1) were obtained from the literature by imposing steady-state constraints in Eq. 6, and/or by fitting the barbed-end profile from Mouneimne et al. (3) (see Fig. 3) and the time course of phosphocofilin from Song et al. (17) (Fig. 2). All experimental data used for parameter fitting are shown in Fig. 2 and details are discussed in the Supporting Material. Parameter sensitivity analysis was done for parameters determined from data fitting. Briefly, we first determined the 95% confidence level from bootstrapping: thus, if we were to choose a set of parameter values within the intervals, very similar results would be obtained. The results are listed in Table 1. Second, we also performed an error analysis on a broad range of parameter values (Fig. S5 in the Supporting Material) and found a relatively narrow region of parameter values that yields a good agreement between model and data (see Supporting Material for details). The most sensitive parameter is R_2, the steady-state level of PIP_2-bound cofilin.

RESULTS

Basic behavior

We simulated the model using default parameter values (Table 1), with variables initialized at the resting/steady-state values (Table S3). EGF stimulation (a pulse in I_{stim}) is turned on at 25 s, and off 60 s later. Parameters for the PLC equation are fit to data in Mouneimne et al. (1), and other parameters are found as described above (and in the Supporting Material). The resulting parameter setting represents a control cell. Dynamics of plc, p_2, the fraction of total cofilin in each form ($v_E c_j^E + v_I c_j^I$), and barbed ends are shown in Fig. 2; concentrations within each compartment are shown in Fig. S9. PLC dynamics (Fig. 2 *A*, *upper left*) closely match data from Mouneimne et al. (1). The scaled PIP_2 (p_2), and PIP_2-bound cofilin (c_2) dynamics agree qualitatively with observed behavior (14). Parameter fitting leads to a barbed-end time course, $b(t)$, that matches the experimentally observed first peak (1) reasonably well. Barbed ends are amplified by an order of magnitude above the basal (resting) value. Only the first barbed-end peak is captured, since this model does not consider Arp2/3. Post-stimulus, there is an ~30 s delay before the sharp increase

TABLE 1 List of parameter values

Parameters	Definition	Values	95% Interval	Source
Cell geometry and diffusion				
V_E	Volume of the membrane-edge compartment	50 μm^3		Cell geometry (see Supporting Material)
V_I	Volume of the interior compartment	950 μm^3		Cell geometry (see Supporting Material)
D	Diffusion coefficient of cofilin	10 $\mu m^2/s$		(36)
l	Thickness of edge compartment	0.2 μm		(24), (see Supporting Material)
EGF stimulation				
I_0	Stimulus amplitude	1.14	1.06–1.44	PLC data fitting
t_{on}	Time at which EGF stimulus starts	25 s		
t_{off}	Time at which EGF stimulus ends	85 s		
PLC and PIP_2 dynamics				
d_{plc}	Basal PLC degradation rate	0.026/s	0.018–0.030	PLC data fitting
d_{hyd}	PLC-induced PIP_2 hydrolysis rate	0.032/s	0.019–0.034	Cofilin data fitting
d_{p2}	Basal PIP_2 hydrolysis rate	0.002/s		(14)
Steady-state fractions of cofilin				
R_2	Fraction bound to PIP_2	0.62	0.49–0.67	Cofilin data fitting
R_a	Fraction of free active form	0.04	0.01–0.11	Cofilin data fitting
R_p	Fraction phosphorylated/inactive	0.20		(17)
R_f	Fraction bound to F-actin	0.11		R_2:$R_f \approx$ 0.85:0.15 (14)
R_m	Fraction bound to G-actin	0.03		Conservation
Cofilin transition rates				
d_{c2}	Basal c_2 release rate (by PIP_2 hydrolysis)	0.002/s		$d_{c2} = d_{p2}$
k_{off}	Unbinding rate from F-actin	0.005/s		(7)
$k_{on}F$	Binding rate to F-actin	0.198/s		Steady-state constraint
k_{mp}	Phosphorylation rate (LIMK)	0.186/s	0.19–0.45	Cofilin data fitting
k_{pm}	Dephosphorylation rate (SSH)	0.03/s		Steady-state constraint
k_{p2}	Binding rate to PIP_2	0.11/s		Steady-state constraint
k_{sev}	Severing rate per cofilin molecule	0.0012/s		Steady-state constraint
n	Degree of cooperativity in severing	4		(21)
ϕ_F	Steady-state value of c_f ($c_{f,ss}$)	2.2		R_f/v_E
Barbed end				
k_{cap}	Barbed-end capping rate	1/s		(24,36,37)
A	Scaling factor for barbed-end generation	4500		Set so that $b = 1$ at rest

Values are estimated from literature sources, from steady-state constraints, or from data fitting. The 95% confidence intervals are obtained by bootstrapping 300 data sets (for details, see discussion in the Supporting Material and Fig. S4).

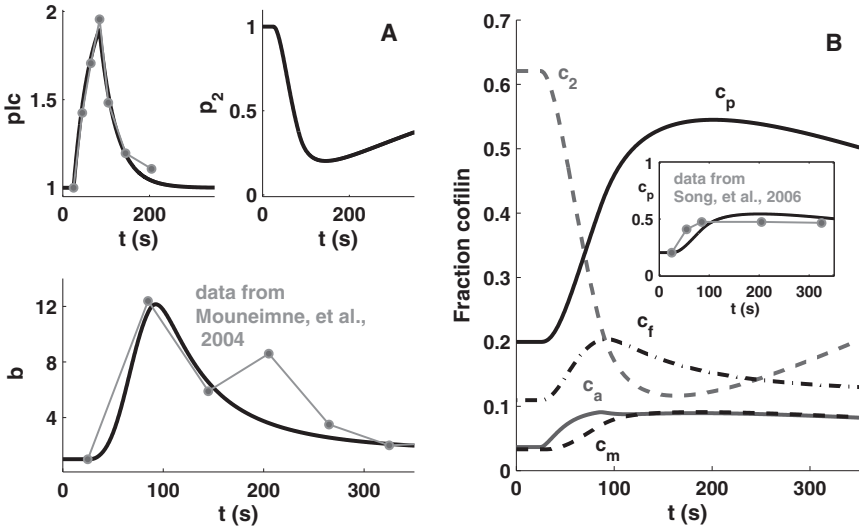

FIGURE 2 Dynamics of the system in response to EGF stimulation. Model results are obtained by simulation using the parameter values listed in Table 1. Experimental data (*line segments connecting dots*) are shown for comparison. (*A*) Time courses of PLC (*plc*), PIP_2 (p_2), and barbed-end (b) levels and data from Mouneimne et al. (1). (*B*) Fraction of total cell cofilin, $v_E c_j^E + v_I c_j^I$, for PIP_2-bound (c_2), F-actin-bound (c_f), G-actin-bound (c_m), phosphorylated (c_p), and active (c_a) cofilin. (*Inset*) Comparison of the simulation result of phosphocofilin, c_p, and experimental data from Song et al. (17).

occurs, so that the peak is attained at ~90 s. The delay is consistent with a second experimental data set shown in Mouneimne et al. (1), where little barbed-end production was observed within 30 s of EGF stimulation.

The delay in the barbed-end peak stems from the time for binding of cofilin to F-actin (to form c_f) and severing of filaments. Although free active cofilin rises immediately poststimulus, F-actin-bound coflilin, c_f, increases only ~10 s later. In turn, G-actin-bound cofilin, c_m, generated after severing, starts to grow at ~20 s. Meanwhile, the level of phosphorylated cofilin, c_p, increases more dramatically than c_f. Note that the temporal profile of c_p, for which we have experimental data (17), is part of the data-fitting process (Fig. 2 *B*, *inset*) and increases from 20% at rest to >50% poststimulus. Observe, however, that the rise of c_p does not yet match the fast experimental rise, as we so far assumed that the phosphorylation rate is constant. We correct this further on.

In Fig. 3, we compare magnitudes of several poststimulus rates, including the F-actin severing rate ($f_{sev}(c_f)$) (first term of Eq. 12), the hydrolysis rate (d_{hyd} (plc − 1)c_2), the net actin-binding rate ($k_{on}Fc_a^E + k_{off}\,c_f$), and the net diffusion of active cofilin out of the edge compartment ($(\omega D/v_E)(c_a^I - c_a^E)$). Diffusion dominates after stimulation: the large flux of c_2 released into the edge compartment creates a large concentration gradient in active cofilin that rapidly diffuses to the cell interior. Phosphorylation and F-actin binding are slower and less pronounced. Thus, the delay in barbed-end generation stems from competition of cofilin binding to F-actin with cofilin diffusion and phosphorylation. As c_f slowly builds up, severing follows. Note that the rate of severing shown in Fig. 3 is lower than other processes. The peak of severing occurs at ~90 s, consistent with the peak of barbed ends.

Effects of LIMK up-/downregulation

We asked how the up-/downregulation of LIMK (the kinase that phosphorylates cofilin) affects the dynamics. This is of particular interest, since overexpression of LIMK has been reported to both enhance and inhibit cell motility (12,25,26). Moreover, upregulation of LIMK expression is also observed in invasive cancer cells, along with increased cofilin activity (27). To study the effect of LIMK expression in our model, we examined how changing k_{mp} (rate of cofilin phosphorylation) by a factor of 2 affects the dynamics.

Increasing k_{mp} leads to a higher steady-state c_p value and thus less severing and fewer barbed ends. However, it also lowers the steady-state barbed-end level, b_{ss}, in such a way that the amplification b_{peak}/b_{ss} actually increases (Fig. 4 *A*). Doubling k_{mp} leads to a >20-fold amplification.

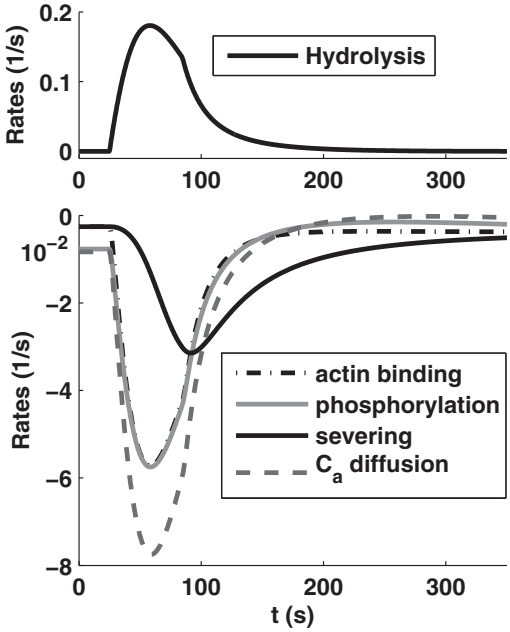

FIGURE 3 A comparison of rates of processes after stimulation. Shown are the hydrolysis rate, $d_{hyd}(plc - 1)c_2$; the net actin binding rate, $-k_{on}F \times c_a^E + k_{off}\,c_f$; the severing rate, $f_{sev}(c_f)$; the net phosphorylation rate, $-k_{mp}c_a^E + k_{pm}c_p^E$; and the diffusion rate of active cofilin, $\omega D/v_E(c_a^I - c_a^E)$.

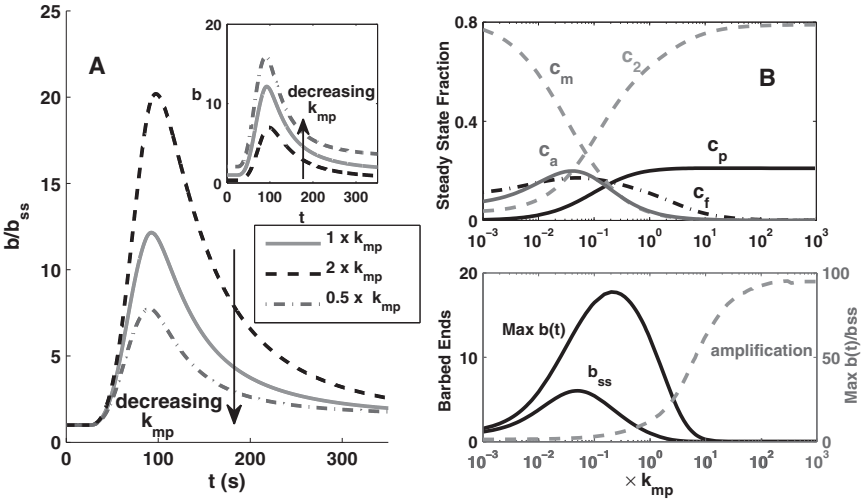

FIGURE 4 Effects of changing the cofilin phosphorylation rate, k_{mp}, reflecting basal LIMK activity, on barbed-end generation. (*A*) Increasing (*black dashed line*) or decreasing (*gray dashed line*) the value of k_{mp} by a factor of 2 from its original value (*solid gray line*) affects the dynamics. (*Inset*) Barbed-end levels relative to baseline ($b(t)/b_{ss}$) and absolute levels ($b(t)$). (*B*) Dependence of steady-state and stimulated levels of variables on the phosphorylation rate, k_{mp}, showing the steady-state fractions of various forms of cofilin versus k_{mp} (*upper*) and the steady-state level (b_{ss}), maximum level (b_{peak} = Max $b(t)$) (*left axis*), and amplification (b_{peak}/b_{ss}) (*right axis*) of barbed ends versus the phosphorylation rate, k_{mp} (*lower*). The horizontal axis is the fold up-/downregulation of the original phosphorylation rate, k_{mp}, in Table 1.

The timing of the barbed-end peak is unchanged. Since phosphorylation liberates cofilin from G/F-actin bound forms, c_m and c_f, increasing k_{mp} also leads to a larger basal c_2, i.e., a greater proportion of cofilin stored in a readily recruitable form is available for release and activation upon stimulation.

Analyzing the steady-state dependence, we find that at very low k_{mp}, steady-state cofilin is dominated by c_m with very little c_2 (Fig. 4 *B*). As k_{mp} increases, c_2 and c_p increase and c_m decreases monotonically. Further, c_f and c_a first increase, then decrease with k_{mp}. This nonmonotonicity leads to a nonmonotonic dependence of steady-state barbed ends (b_{ss}) and transient peak (b_{peak}) on k_{mp} (Fig. 4 *B*, *lower*). Initially, as k_{mp} is increased, more PIP_2-bound cofilin is available to be released so that the barbed-end levels at rest and after stimulation also increase. At the higher range ($k_{mp} > k_{on}F$), phosphorylation robs activated cofilin before it can bind to and sever F-actin. These results imply that regulation of cofilin by the basal level of LIMK plays a role not only in limiting the action of severing, but also in both up- and downregulation of barbed-end amplification.

Dynamics of LIMK

Absent in the model so far are the dynamics of LIMK and SSH poststimulation by EGF. Partly due to that simplification, c_p dynamics (Fig. 2, *inset*) were so far not closely matched to the experimental data, despite the fitting procedure. Song et al. (17) showed that active/phosphorylated LIMK doubles and stays elevated for 360 s poststimulation. The (unmeasured) level of SSH can be inferred to rise since the phosphocofilin level also remained elevated at 360 s after stimulation (17). We asked how such LIMK/SSH dynamics could affect our conclusions.

To avoid significantly increasing the model complexity, we simply fit a time-varying function $f(t)$ to the LIMK data in Song et al. (17) (Fig. 5, *upper*). We assumed that LIMK = $k_{mp} \times f(t)$ and SSH = $k_{pm} \times f(t)$, i.e., that LIMK and SSH activities were proportional to $f(t)$.

We compare the output for dynamic LIMK, dynamic LIMK-SSH, and the original model in Fig. 5. In the first case ($k_{mp} \times f(t)$, k_{pm} = constant), b_{peak} is only half of its value in the basic model. This model variant has rampant cofilin phosphorylation due to the poststimulus rise of LIMK activity. Thus, active cofilin, c_a, can hardly build up (Fig. 5, *lower right*), so there is less cofilin binding to F-actin, less severing, and thus a lower b_{peak}. With both LIMK and SSH dynamics, amplification is ~8. The dynamics of cofilin forms (Fig. S10), particularly those in the interior compartment, are fairly similar across the three model variants, with the level of c_a showing the greatest impact of dynamic LIMK.

We also explored the possibility that the edge compartment is protected from phosphorylation, as suggested by data from Song et al. (17), by setting $k_{mp} = k_{pm} = 0$ in the edge compartment in the same dynamic LIMK/SSH model variant (Fig. 6). The steady-state value of c_2 is slightly lower whereas c_f and b_{ss} are elevated. Barbed-end amplification is ~10-fold (Fig. 6, *upper*). As expected, the build-up of c_p^E is retarded when LIMK activity is minimal in the edge compartment. Including SSH dynamics leads to cell-interior cofilin dynamics similar to those of the original model (Fig. 6, *lower*).

A comparison with previous results (Fig. 5) shows that with membrane-edge protection, barbed ends peak more quickly (at a rate similar to that of the original model) but then also drop more quickly after peaking. We attribute the decrease in barbed-end amplification here not only to the drop in c_2 level ready for release but also to the lack of reactivation occurring within the edge compartment after the first round of severing. This is shown in Fig. 6 (*middle*), where we plotted the level of c_f scaled by its basal/steady-state level. Thus, early barbed-end production is sensitively tuned to events within the small edge compartment of the

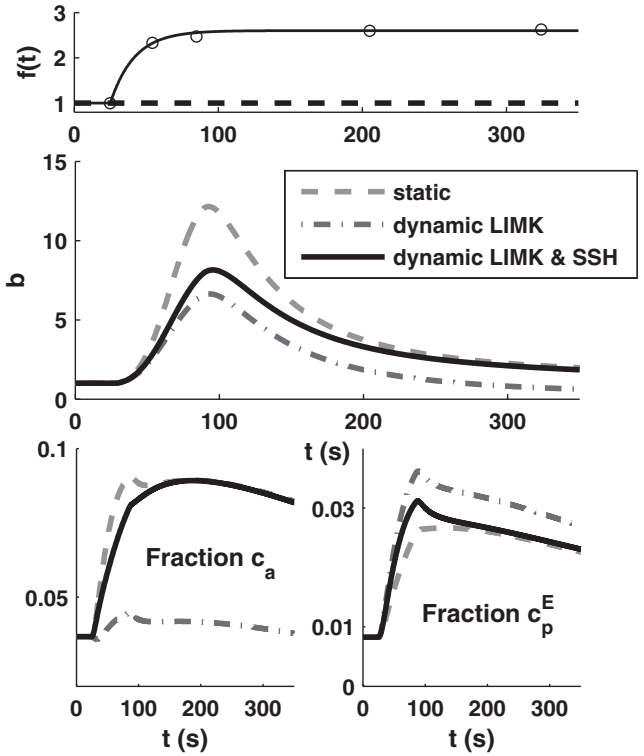

FIGURE 5 Effects of dynamic LIMK and SSH response to stimulation in model and experimental data (indicated below instead). (*Upper*) Phosphorylation and dephosphorylation were both assumed to be $k_{mp} \times f(t)$ and $k_{pm} \times f(t)$, with $f(t) = 1 + 1.6(1 - \exp(0.06\,t))$; this function was chosen to fit data (*open dots*) from Song et al. (17). (*Middle*) Dynamics of barbed-end profile for the original model/static case (constant k_{mp} and k_{pm}) (*dashed gray line*), the dynamic LIMK case ($k_{mp} \times f(t)$ only) (*dash-dotted line*), and dynamic LIMK and SSH ($k_{mp} \times f(t)$ and $k_{pm} \times f(t)$) (*solid line*). (*Lower*) Dynamics of free active (*left*) and phosphorylated (*right*) cofilin on the edge compartment.

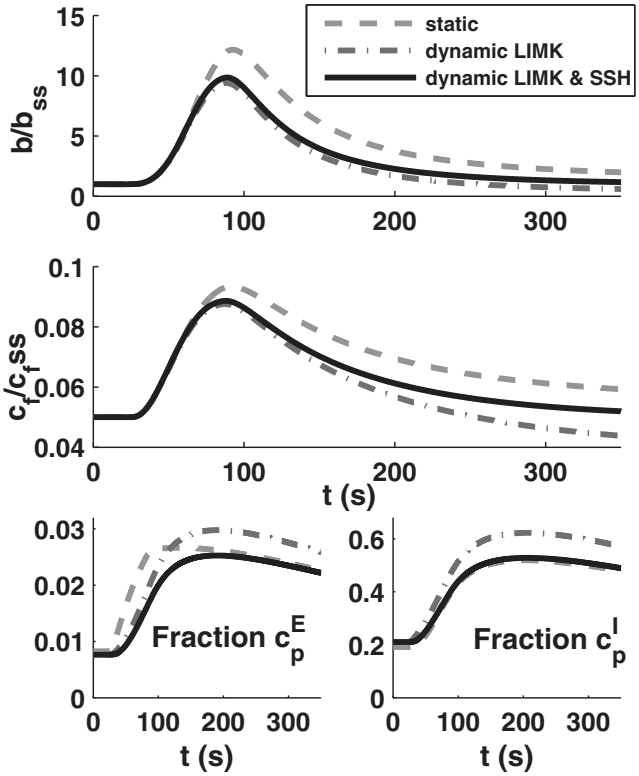

FIGURE 6 Effects of membrane edge protection where no phosphorylation/dephosphorylation occurs within the edge compartment ($k_{mp} = k_{pm} = 0$ at edge). In the interior compartment, dynamic LIMK and SSH responses to stimulation are considered as in Fig. 5. (*Upper*) Barbed ends ($b(t)/b_{ss}$). (*Middle*) Relative level of c_f available for severing (c_f scaled by its steady-state level, $c_{f,\,ss}$). (*Lower*) Dynamics of phosphocofilin fractions in the edge and interior compartments.

cell and is relatively insensitive to the cofilin dynamics in the bulk interior of the cell.

DISCUSSION

In addition to recycling old actin filaments, cofilin plays an important role in initiating cell movement by severing filaments and generating new barbed ends. Our two-compartment ordinary-differential-equation model of cofilin dynamics downstream of EGF stimulation in cancer cells reproduces the early transient actin filament barbed-end production observed experimentally, and dissects the cofilin-induced F-actin severing into underlying steps. The model allows us to estimate rates of transition between various forms of cofilin by matching predictions and experimental data for both resting levels and stimulated levels of measurable quantities. Further, the model predicts the levels of variables (such as the fraction of active cofilin) that are currently beyond experimental resolution. The model demonstrates that the response of the system is most strongly affected by 1), the fraction of PIP_2-bound cofilin (c_2) in the resting cell available for release; and 2), the rate of binding and severing of F-actin relative to competing processes such as cofilin phosphorylation or diffusion. Another important take-home lesson is that upregulating the cofilin regulator LIMK can actually lead to a more amplified response to EGF stimulation, i.e., a greater amplification in barbed-end production poststimulation, even though the primary role of LIMK is to deactivate cofilin.

An essential component of our model is a strong nonlinearity in the severing rate as a function of active cofilin. In fact, we believe that the cofilin-actin cooperative binding kinetics (21,22) is responsible for generating the transient 10- to 15-fold barbed-end amplification (1). This assumption is consistent with previous in vitro and modeling studies on cofilin-actin binding (21,28,29), which show that cofilin binds cooperatively to F-actin with Hill-like kinetics of degree $n = 4$–10. We explored a range of values of n and found that a fit to the experimental data within the 95% confidence interval could be achieved with values of $4 \leq n \leq 10$. We chose the value $n = 4$ as it yielded one of the best fits. Cofilin binding changes the flexibility of actin filaments, allowing more cofilin to bind; the enhanced bending flexibility also promotes severing (22,30,31). It is

conjectured, but not yet confirmed, that mechanical tension at the cell edge may also affect cofilin dynamics (E. De La Cruz, Yale University, personal communication, 2011).

In building our model, we used mostly data from mammary carcinoma cells in vivo. Direct in vitro measurement is largely lacking, hindering the estimation of dephosphorylation and phosphorylation rates of cofilin. Having a finer temporal measurement of simultaneous levels of variables would be helpful in data fitting and in resolving the exact temporal dynamics.

From our parameter sensitivity study, we also found a critical parameter, namely the basal amount of PIP_2-bound cofilin ($c_2 \approx 0.6$ at rest) needed to faithfully reproduce the experimental data. This means that ~60% of total cofilin should be in the PIP_2-bound form in the resting cell for dynamics consistent with observations. This is possible given the localization of cofilin with PIP_2 observed in carcinoma cells (14). Although a large barbed-end amplification is possible at a lower level of c_2, the level of phosphocofilin cannot then increase to the level observed experimentally (17).

Limitations of this model include the very coarse spatial representation (two compartments only) and inclusion of few key intermediates. We did not model here the dynamics of F-actin that takes place once the newly formed barbed ends start to grow and extend. In experiments, F-actin has been found to increase by less than twofold within 60 s after EGF stimulation. A more significant increase occurs later, once Arp2/3 activity is promoted (23) (not currently modeled). The second peak of barbed ends stems from Arp2/3-mediated F-actin branching (1). Tests of the model with a dynamic F-actin variable showed minimal effect beyond that described here and was deemed insignificant relative to other processes on the timescale of 1 min.

Cofilin has other roles that we did not include here. In vitro studies have shown that, depending on conditions, ADF/cofilin (at low concentrations) severs but (at higher levels) depolymerizes F-actin (6–9). The latter helps to recycle G-actin and promote rapid barbed-end growth (10,32,33). Other effects of cofilin include release of the phosphate groups from F-actin, promoting dissociation of Arp2/3 complexes from ADP-F-actin and consequent debranching of filaments (6,34). At a very high concentration ($>10\ \mu$M), cofilin can also nucleate filaments de novo (6). In the interest of keeping the first models tractable, such effects were not modeled here. These could form extensions of the basic model as a future step.

Our results strongly suggest that the level of barbed-end production is mainly dependent on events occurring within a thin compartment abutting the cell membrane rather than the large interior cytosolic compartment. Comparing the two- versus one-compartment model (where there is no distinction between cell edge and interior), we found that the latter significantly underestimates the barbed-end peak, and the time course of its rising phase (see Supporting Material). Spatial localization is crucial, as cofilin binding to F-actin is restricted to the edge compartment, where filaments are not protected by tropomyosin and where cofilin phosphorylation may be low. If this is true, then, as we have shown, upon release from the membrane, active cofilin strongly targets F-actin rather than being diverted to competing processes. We then attain the same rate of barbed-end production even in the concurrent presence of upregulated LIMK activity. As spatial localization appears to play an important role in determining the response of the system, further modeling based on a spatially extended system that can describe cofilin gradients forms a promising future direction.

Thus far in this model, we have considered only the action of cofilin (and first barbed-end peak) and not the dynamics of Arp2/3 associated with a second peak of barbed ends. Whereas cofilin binds preferentially to ADP-actin rather than ATP-actin monomers (7,11), Arp2/3 has a higher affinity to ATP-actin filaments. Thus, cofilin severing, which allows for new F-actin growth, also promotes subsequent filament branching by Arp2/3 (1–3). Hence, cofilin and Arp2/3 activities work in synergy to create a large increase in actin polymerization (35). Testing the boundaries of this synergy forms another interesting future direction.

APPENDIX: LIST OF EQUATIONS IN NONDIMENSIONAL FORM

PLC level:

$$\begin{aligned} \frac{dplc}{dt} &= d_{plc}(I_{stim}(t) + 1 - plc) \ \text{ with} \\ I_{stim}(t) &= I_{stim0} \times H(t - t_{on}) \times H\big(t - t_{off}\big), \end{aligned} \tag{7}$$

where H(t) is the Heaviside function.

PIP_2 level:

$$\frac{dp_2}{dt} = d_{p2}(1 - p_2) - d_{hyd}(plc - 1)p_2; \tag{8}$$

PIP_2-bound cofilin:

$$\frac{dc_2}{dt} = k_{p2}\, p_2\, c_p - d_{c2}c_2 - d_{hyd}(plc - 1)c_2; \tag{9}$$

Active cofilin in the edge compartment:

$$\begin{aligned} \frac{dc_a^E}{dt} &= d_{c2}c_2 + k_{off}c_f - k_{on}F\, c_a^E - k_{mp}c_a^E + k_{pm}c_p^E \\ &\quad + d_{hyd}(plc - 1)c_2 + \frac{\omega D}{V_E}\big(c_a^I - c_a^E\big); \end{aligned} \tag{10}$$

F-actin-bound cofilin in the edge compartment:

$$\frac{dc_f}{dt} = k_{on}F\, c_a^E - k_{off}c_f - k_{sev}\phi_F\left(\frac{c_f}{\phi_F}\right)^n; \tag{11}$$

G-actin-bound cofilin in the edge compartment:

$$\frac{dc_m^E}{dt} = k_{sev}\phi_F\left(\frac{c_f}{\phi_F}\right)^n - k_{mp}c_m^E + k_{pm}c_p^E + \frac{\omega D}{V_E}\big(c_m^I - c_m^E\big); \tag{12}$$

Phosphorylated cofilin in the edge compartment:

$$\frac{dc_p^E}{dt} = k_{mp}\left(c_a^E + c_m^E\right) - 2k_{pm}c_p^E - k_{p2}\,p_2\,c_p^E + \frac{\omega D}{V_E}\left(c_p^I - c_p^E\right); \quad (13)$$

Active cofilin in the interior compartment:

$$\frac{dc_a^I}{dt} = -k_{mp}c_a^I + k_{pm}c_p^I + \frac{\omega D}{V_I}\left(c_a^E - c_a^I\right); \quad (14)$$

G-actin-bound cofilin in the interior compartment:

$$\frac{dc_m^I}{dt} = -k_{mp}c_m^I + k_{pm}c_p^I + \frac{\omega D}{V_I}\left(c_m^E - c_m^I\right); \quad (15)$$

Phosphorylated cofilin in the interior compartment:

$$\frac{dc_p^I}{dt} = k_{mp}\left(c_a^I + c_m^I\right) - 2k_{pm}c_p^I + \frac{\omega D}{V_I}\left(c_p^E - c_p^I\right); \quad (16)$$

Barbed-end production:

$$\frac{db}{dt} = k_{cap}(1-b) + A\,k_{sev}\phi_F\left(\frac{c_f}{\phi_F}\right)^n. \quad (17)$$

SUPPORTING MATERIAL

Ten figures, four tables, additional text, and references are available at http://www.biophysj.org/biophysj/supplemental/S0006-3495(11)00254-2.

We are grateful to Raibatak Das, Daniel Coombs, Dan Larson, and Enrique De La Cruz for comments and advice, and to Robert Eddy for unpublished PIP_2 data.

This research was supported by a subcontract (to L.E.K.) from the National Institutes of Health (Grant No. R01 GM086882) to Anders Carlsson, Washington University, and by a Natural Sciences and Engineering Research Council discovery grant (to L.E.K.). J.C. is funded by National Institutes of Health grant CA150344. E.P. was supported by an International Graduate Training Center fellowship from the Pacific Institute for the Mathematical Sciences (Canada).

REFERENCES

1. Mouneimne, G., L. Soon, …, J. Condeelis. 2004. Phospholipase C and cofilin are required for carcinoma cell directionality in response to EGF stimulation. *J. Cell Biol.* 166:697–708.
2. Ghosh, M., X. Song, …, J. S. Condeelis. 2004. Cofilin promotes actin polymerization and defines the direction of cell motility. *Science.* 304:743–746.
3. Mouneimne, G., V. DesMarais, …, J. Condeelis. 2006. Spatial and temporal control of cofilin activity is required for directional sensing during chemotaxis. *Curr. Biol.* 16:2193–2205.
4. Sidani, M., D. Wessels, …, J. Condeelis. 2007. Cofilin determines the migration behavior and turning frequency of metastatic cancer cells. *J. Cell Biol.* 179:777–791.
5. Ichetovkin, I., W. Grant, and J. Condeelis. 2002. Cofilin produces newly polymerized actin filaments that are preferred for dendritic nucleation by the Arp2/3 complex. *Curr. Biol.* 12:79–84.
6. Andrianantoandro, E., and T. D. Pollard. 2006. Mechanism of actin filament turnover by severing and nucleation at different concentrations of ADF/cofilin. *Mol. Cell.* 24:13–23.
7. Blanchoin, L., and T. D. Pollard. 1999. Mechanism of interaction of Acanthamoeba actophorin (ADF/Cofilin) with actin filaments. *J. Biol. Chem.* 274:15538–15546.
8. Carlier, M.-F., V. Laurent, …, D. Pantaloni. 1997. Actin depolymerizing factor (ADF/cofilin) enhances the rate of filament turnover: implication in actin-based motility. *J. Cell Biol.* 136:1307–1322.
9. Pope, B. J., S. M. Gonsior, …, A. G. Weeds. 2000. Uncoupling actin filament fragmentation by cofilin from increased subunit turnover. *J. Mol. Biol.* 298:649–661.
10. van Rheenen, J., J. Condeelis, and M. Glogauer. 2009. A common cofilin activity cycle in invasive tumor cells and inflammatory cells. *J. Cell Sci.* 122:305–311.
11. Blanchoin, L., and T. D. Pollard. 1998. Interaction of actin monomers with Acanthamoeba actophorin (ADF/cofilin) and profilin. *J. Biol. Chem.* 273:25106–25111.
12. Oser, M., and J. Condeelis. 2009. The cofilin activity cycle in lamellipodia and invadopodia. *J. Cell. Biochem.* 108:1252–1262.
13. Wang, W., R. Eddy, and J. Condeelis. 2007. The cofilin pathway in breast cancer invasion and metastasis. *Nat. Rev. Cancer.* 7:429–440.
14. van Rheenen, J., X. Song, …, J. S. Condeelis. 2007. EGF-induced PIP2 hydrolysis releases and activates cofilin locally in carcinoma cells. *J. Cell Biol.* 179:1247–1259.
15. Gorbatyuk, V. Y., N. J. Nosworthy, …, G. F. King. 2006. Mapping the phosphoinositide-binding site on chick cofilin explains how PIP2 regulates the cofilin-actin interaction. *Mol. Cell.* 24:511–522.
16. Moriyama, K., K. Iida, and I. Yahara. 1996. Phosphorylation of Ser-3 of cofilin regulates its essential function on actin. *Genes Cells.* 1:73–86.
17. Song, X., X. Chen, …, R. J. Eddy. 2006. Initiation of cofilin activity in response to EGF is uncoupled from cofilin phosphorylation and dephosphorylation in carcinoma cells. *J. Cell Sci.* 119:2871–2881.
18. Ojala, P. J., V. Paavilainen, and P. Lappalainen. 2001. Identification of yeast cofilin residues specific for actin monomer and PIP2 binding. *Biochemistry.* 40:15562–15569.
19. Tobacman, L. S., and E. D. Korn. 1983. The kinetics of actin nucleation and polymerization. *J. Biol. Chem.* 258:3207–3214.
20. Mullins, R. D., J. A. Heuser, and T. D. Pollard. 1998. The interaction of Arp2/3 complex with actin: nucleation, high affinity pointed end capping, and formation of branching networks of filaments. *Proc. Natl. Acad. Sci. USA.* 95:6181–6186.
21. De La Cruz, E. M. 2005. Cofilin binding to muscle and non-muscle actin filaments: isoform-dependent cooperative interactions. *J. Mol. Biol.* 346:557–564.
22. McGough, A., B. Pope, …, A. Weeds. 1997. Cofilin changes the twist of F-actin: implications for actin filament dynamics and cellular function. *J. Cell Biol.* 138:771–781.
23. DesMarais, V., I. Ichetovkin, …, S. E. Hitchcock-DeGregori. 2002. Spatial regulation of actin dynamics: a tropomyosin-free, actin-rich compartment at the leading edge. *J. Cell Sci.* 115:4649–4660.
24. Mogilner, A., and L. Edelstein-Keshet. 2002. Regulation of actin dynamics in rapidly moving cells: a quantitative analysis. *Biophys. J.* 83:1237–1258.
25. Bagheri-Yarmand, R., A. Mazumdar, …, R. Kumar. 2006. LIM kinase 1 increases tumor metastasis of human breast cancer cells via regulation of the urokinase-type plasminogen activator system. *Int. J. Cancer.* 118:2703–2710.
26. Hotulainen, P., E. Paunola, …, P. Lappalainen. 2005. Actin-depolymerizing factor and cofilin-1 play overlapping roles in promoting rapid F-actin depolymerization in mammalian nonmuscle cells. *Mol. Biol. Cell.* 16:649–664.
27. Wang, W., J. B. Wyckoff, …, J. S. Condeelis. 2007. Coordinated regulation of pathways for enhanced cell motility and chemotaxis is conserved in rat and mouse mammary tumors. *Cancer Res.* 67:3505–3511.

28. Cao, W., J. P. Goodarzi, and E. M. De La Cruz. 2006. Energetics and kinetics of cooperative cofilin-actin filament interactions. *J. Mol. Biol.* 361:257–267.

29. Prochniewicz, E., N. Janson, …, E. M. De la Cruz. 2005. Cofilin increases the torsional flexibility and dynamics of actin filaments. *J. Mol. Biol.* 353:990–1000.

30. De La Cruz, E. M. 2009. How cofilin severs an actin filament. *Biophys Rev.* 1:51–59.

31. McCullough, B. R., L. Blanchoin, …, E. M. De la Cruz. 2008. Cofilin increases the bending flexibility of actin filaments: implications for severing and cell mechanics. *J. Mol. Biol.* 381:550–558.

32. Bamburg, J. R. 1999. Proteins of the ADF/cofilin family: essential regulators of actin dynamics. *Annu. Rev. Cell Dev. Biol.* 15:185–230.

33. Pantaloni, D., C. Le Clainche, and M.-F. Carlier. 2001. Mechanism of actin-based motility. *Science.* 292:1502–1506.

34. Chan, C., C. C. Beltzner, and T. D. Pollard. 2009. Cofilin dissociates Arp2/3 complex and branches from actin filaments. *Curr. Biol.* 19: 537–545.

35. DesMarais, V., F. Macaluso, …, M. Bailly. 2004. Synergistic interaction between the Arp2/3 complex and cofilin drives stimulated lamellipod extension. *J. Cell Sci.* 117:3499–3510.

36. Pollard, T. D., L. Blanchoin, and R. D. Mullins. 2000. Molecular mechanisms controlling actin filament dynamics in nonmuscle cells. *Annu. Rev. Biophys. Biomol. Struct.* 29:545–576.

37. Dawes, A. T., G. Bard Ermentrout, …, L. Edelstein-Keshet. 2006. Actin filament branching and protrusion velocity in a simple 1D model of a motile cell. *J. Theor. Biol.* 242:265–279.

Supplementary Material

A Temporal Model of Cofilin Regulation and the Early Peak of Actin Barbed Ends in Invasive Tumor Cells

Nessy Tania[a], Erin Prosk[a], John Condeelis[b], and Leah Edelstein-Keshet[a1]

[a]Department of Mathematics,
University of British Columbia, Vancouver, BC V6T 1Z2, Canada

[b]Department of Anatomy and Structural Biology,
Gruss Lipper Biophotonics Center,
Albert Einstein College of Medicine of Yeshiva University, Bronx, NY 10461

[1]Corresponding author
Department of Mathematics, University of British Columbia
Room 121, 1984 Mathematics Road, Vancouver, BC V6T 1Z2, Canada.
Phone: 1-604-822-5889. *Fax:* 1-604-822-6074. *Email:* keshet@math.ubc.ca

Contents

1 Nonlinear kinetics of severing **2**
Fig. S1: Cofilin-Barbed end dynamics in Eqs. (S3-S4) for various severing functions . 3

2 One-Compartment Cofilin Dynamics Model **5**
Fig. S2: Schematics of the single compartment ODE model for cofilin regulation. . 5

3 Two-Compartment Cofilin Dynamics Model **6**
Fig. S3: Cell geometry used in the two-compartment model. 6
Diffusion Flux Between Compartments 7
List of Equations in Dimensional/Unit-Carrying Form 8

4 Determination of Parameter Values **9**
Parameter Determination from Steady State Constraint 9
Parameter Fitting Procedure 10
Fig. S4: Distribution of parameter values from bootstrapping with 300 data sets . . 10
Fig. S5: A good fit to barbed ends (top) and phospho-cofilin (bottom) data is obtained only if the resting cell has a high level of PIP_2-bound cofilin ($R_2 = v_E c_{2,SS}$ is large). 11
Sensitivity to Parameter Values 12

5 Comparing the One and Two- Compartment Models **12**
List of One-Pool Model Equations in Nondimensional Forms 12
Comparison of Results: Effects of Localization 13
Fig. S6: Effect of localization: a comparison of results from the two- versus one-compartment models. 14
Fig. S7: As in Fig. S6 but with a 20 times reduction in phosphorylation rate k_{mp}. . 14
Fig. S8: Barbed end profiles obtained from the two compartment model with various edge compartment volumes. 14

6 Results: Additional Figures **15**
Fig. S9: Nondimensional concentrations of cofilin forms 16
Fig. S10: Dynamics of cofilin fractions for the time-varying LIMK and/or SSH . . . 17

1 Nonlinear kinetics of severing

In this section, we explain in detail how we chose the nonlinear function that describes the kinetics of actin filament severing by cofilin (given by Eqn (1) in the main text). This function has to be able to account for how amplification of barbed ends can be produced due to cofilin binding cooperativity. We consider the minimal model in which only the active cofilin level, $C(t)$ and the barbed end density, $B(t)$ are tracked. (Eqs (1,2) in the main text, repeated here for convenience:)

$$\frac{dC}{dt} = \bar{I}_{stim}(t) + I_C - k_p C - F_{sev}(C), \tag{S1}$$

$$\frac{dB}{dt} = I_B - k_{cap} B + \bar{A} F_{sev}(C), \tag{S2}$$

where, I_B and I_C denotes basal rates of production and k_p and k_{cap} the basal rates of degradation and capping. Following a time-dependent stimulus, $\bar{I}_{stim}(t)$, barbed ends are generated when cofilin severs F-actin at the rate $F_{sev}(C)$. F-actin is assumed to be constant and not a limiting factor. The constant $\bar{A}$ in the severing term in the equation for B represents a scale factor for change of units between C, generally given in μM, and the barbed end density, B, is given in units of $\#/\mu\text{m}^2$. A concentration of 1 μM corresponds to approximately 600 molecules/μm^3. For a region of interest (e.g. a lamellipod) of thickness of 0.15 μm, a concentration of 1 μM gives $A = 0.15 \cdot 600 \approx 100$ molecules per 1 μm^2.

When cofilin activity is minimal, we expect the barbed end production rate, $\bar{A} F_{sev}(C)$, to be small. Thus, without stimulation, the rest/steady-state value of B can be approximated by $B^* = I_B/k_{cap}$. To reduce the number of parameters, we scale Eqn. (S2) and consider the non-dimensional quantity $b(t) = B(t)/B^*$ whose dynamics follow

$$\frac{db}{dt} = A f_{sev}(c) + k_{cap}(1 - b). \tag{S3}$$

Eqn. (S1) for C can similarly be scaled by defining $C^* = I_C/k_p$, which results in the following equation for $c(t) = C(t)/C^*$,

$$\frac{dc}{dt} = I_{stim}(t) + k_p(1 - c) - f_{sev}(c). \tag{S4}$$

A, $f_{sev}(c)$ and $I_{stim}(t)$ are the corresponding scaled version of $\bar{A}$, $F_{sev}(C)$, and $\bar{I}_{stim}(t)$ respectively. When $c = 0$, the barbed ends rest level is $b_{ss} = 1$ and amplification is defined as the fold-multiple of this value at the peak or barbed ends, b_{peak}. The definition of the parameters as well as the numerical values used for the non-dimensional model are given in Table S1.

We now study the response of the system when various types of severing functions $f_{sev}(c)$ are used. In all cases, $f_{sev}(c)$ is constructed such that the steady state of the system remains the same. Then, at steady-state, there is very little severing occurring, $f_{sev} = k_{sev}\, c_{ss} << 1$, where c_{ss} is the steady state value of c. Specifically, we consider the following three functions:

(a) A linear severing function,

$$f_{sev}(c) = k_{sev}\, c\,. \tag{S5}$$

Table S1: List of parameters for the minimal model given in Eqs. (S3-S4). Note that parameter values here are chosen to approximately yield the peak of barbed ends seen experimentally (2) and do not reflect the final choice of parameter values used in the detailed cofilin cycle model.

Parameter	Definition	Value
A	scale factor for unit conversions from C to B	$100/\mu\text{m}^2$
k_{cap}	barbed end capping rate	1 /s
k_p	rate of cofilin inactivation/phosphorylation	1 /s
k_{sev}	cofilin mediated severing rate	0.01 /s
n	degree of cooperativity	7

(b) A nonlinear severing function with saturation,

$$f_{sev}(c) = g_{max}\, k_{sev}\, c_{ss} \left(\frac{c^n}{c^n + k_n^n} \right) . \tag{S6}$$

To have $f_{sev} = k_{sev}\, c_{ss}$ at rest, we set $g_{max} = (c_{ss}^n + k_n^n)/c_{ss}^n$. This severing term approximates sequential cooperative binding and the quasi-equilibrium approximation for the following reaction scheme,

$$n \text{ Active Cofilin} + \text{F-actin} \rightarrow \text{Barbed-end} + n \text{ Inactive Cofilin} . \tag{S7}$$

Then, k_n is the dissociation constant for cofilin-actin binding. Other studies have reported that cofilin binds to actin filaments cooperatively as binding changes the structure of the actin filament allowing for further cofilin binding. The binding process can be described by a Hill function of degree 4-10 (1).

(c) A nonlinear severing function with no saturation,

$$f_{sev}(c) = k_{sev}\, c_{ss} \left(\frac{c}{c_{ss}} \right)^n . \tag{S8}$$

This function approximates the behaviour of (S6) for $c \ll k_n$.

To simplify analysis, we set $I_{stim} = 0, b(0) = b_{ss} = 1$ and study the response to various initial levels of $c(0)$ above the normal resting value of $c_{ss} \approx 1$. This represents an initial elevation of cofilin downstream of a stimulus pulse. We then track the change in b relative to its steady-state value. The results are shown in phase-plane plots in Fig. S1. The maximal height of the black curves above $b_{ss} = 1$ in the cb plane can be interpreted as the amplification of barbed ends, i.e., as b_{peak}/b_{ss}. We can thus compare the amplification obtained with a variety of assumptions about the severing kinetics.

For a linear severing function, the degree of barbed-end amplification is weak. For example, increasing cofilin five-fold only results in amplification by a factor of about 2

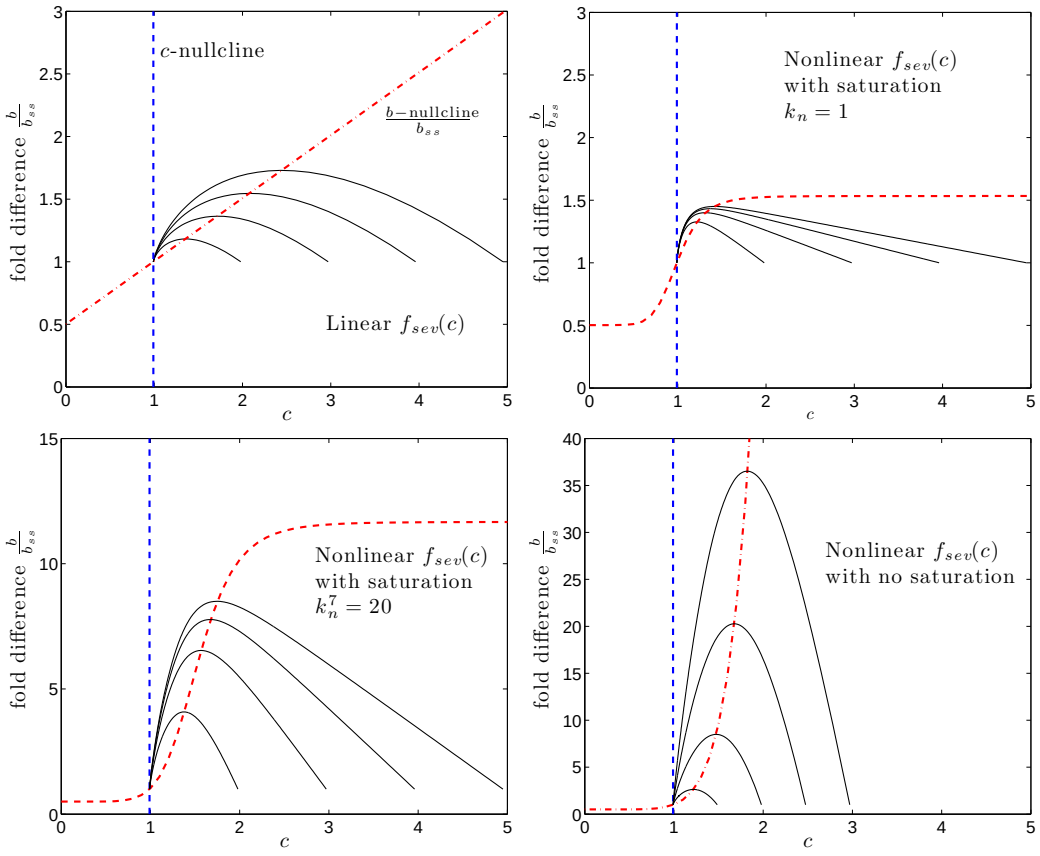

Figure S1: Phase plane behavior of cofilin and barbed end amplification in the two-variable system with severing functions $f_{sev}(c)$ (a-c). Dashed lines indicate nullclines of Eqs. (S3-S4), and solid lines are sample trajectories starting from various elevated levels of cofilin. Amplification is the difference between the maximal height of the black curves and the steady state barbed ends level $b_{ss} = 1$.

($b_{peak} \approx 2b_{ss}$). We can also determine the amount of amplification by treating cofilin, c as a parameter. As c is varied, the "steady-state" level of b is given by

$$b^* = \frac{A f_{sev}(c) + k_{cap}}{k_{cap}}\,. \tag{S9}$$

(This equation also corresponds to the b-nullcline of the full system). If $f_{sev}(c)$ is linear, then changing c by two-fold will at most leads to the doubling of b^*. Thus, to have a large degree of amplification, as observed experimentally, a non-linear severing rate is required. For a Hill function, $f_{sev}(c)$ (Eqn. (S6)), the maximum barbed-end amplification is determined by the saturated level, ($g_{max}\, k_{sev}\, c_{ss}$). Larger degree of amplification is observed as k_n is increased. In the limit of k_n very large relative to the range of c, the severing function no longer saturates and is exactly given by Eqn. (S8) (this is the range far from saturation). This explains our choice of (S8) for the severing function f_{sev} in the models.

2 One-Compartment Cofilin Dynamics Model

We here briefly present the one-compartment model, schematically shown in Fig S2. This model is the first correction of the mini-model presented in the previous section. Here, the cofilin activity cycle, modulated by PIP_2 binding, actin binding, and phosphorylation are taken into account. The equations describing the single compartment model are listed below, and simulation results are later compared with the more detailed two-compartment model using a scaled (dimensionless) model formulation.

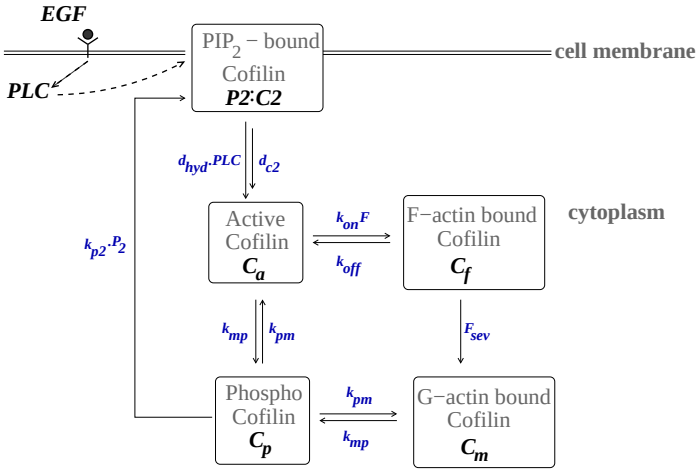

Figure S2: Schematics of the single compartment ODE model for cofilin regulation. Here, the cell is assumed to consist only of one single well-mixed compartment. C_2 is the cofilin fraction bound to PIP_2 on the membrane, C_a is active cofilin in the cytosol, C_f is the fraction bound to F-actin, C_m reflects G-actin-monomer bound cofilin, and C_p is phosphorylated/inactive cofilin.

Equations for the One-Compartment Model

PLC Activity

$$\frac{dPLC}{dt} = \bar{I}_{stim}(t) + I_{plc} - d_{plc}PLC\,, \tag{S10}$$

with the EGF stimulation profile

$$\bar{I}_{stim}(t) = \bar{I}_{stim0} \cdot [H(t - t_{on}) - H(t - t_{off})]\,, \tag{S11}$$

where $H(s)$ is the Heaviside function (i.e. unit step function that turns on at $t = 0$).

PIP_2 level

$$\frac{dP_2}{dt} = I_{p_2} - d_{p_2}P_2 - d_{hyd}\left(\frac{PLC - PLC_{rest}}{PLC_{rest}}\right)P_2\,. \tag{S12}$$

PIP_2-bound cofilin

$$\frac{dC_2}{dt} = k'_{p_2}\left(\frac{P_2}{P_{2,rest}}\right)C_p - d_{c_2}C_2 - d_{hyd}\left(\frac{PLC - PLC_{rest}}{PLC_{rest}}\right)C_2\,. \tag{S13}$$

Active cofilin

$$\frac{dC_a}{dt} = d_{c2}C_2 + d_{hyd}\left(\frac{PLC - PLC_{rest}}{PLC_{rest}}\right)C_2 - k'_{on}F\,C_a + k_{off}C_f - k_{mp}C_a + k_{pm}C_p\,. \tag{S14}$$

F-actin-bound cofilin

$$\frac{dC_f}{dt} = k'_{on}F\,C_a - k_{off}C_f - F_{sev}(C_f)\,, \tag{S15}$$

with the severing function

$$F_{sev}(C_f) = k_{sev}\,C_{f,rest}\left(\frac{C_f}{C_{f,rest}}\right)^n\,. \tag{S16}$$

G-actin-bound cofilin

$$\frac{dC_m}{dt} = F_{sev}(C_f) - k_{mp}C_m + k_{pm}C_p\,. \tag{S17}$$

Phosphorylated cofilin

$$\frac{dC_p}{dt} = k_{mp}(C_a + C_m) - 2k_{pm}C_p - k'_{p_2}\left(\frac{P_2}{P_{2,rest}}\right)C_p\,. \tag{S18}$$

Barbed end production

$$\frac{dB}{dt} = \bar{A}F_{sev}(C_F) - k_{cap}B\,, \tag{S19}$$

Parameters for a (dimensionless form of) this model are as shown in Table S4. The notation for the parameters k'_{on} and k'_{p2} is explained in connection with a comparison between the one and the two pool models. (Briefly, to compare the two models, we set $k'_{on} = k_{on}V_E/V_{tot}$ and $k'_{p_2} = k_{p_2}V_E/V_{tot}$ where volumes are explained in the next section.)

3 Two-Compartment Cofilin Dynamics Model

Here we discuss the geometry of the two-compartment model. Fig. S3 shows a magnified view of the inset in Fig. 1 of the main paper. The edge compartments (representing a nascent lamellipod) is approximated as a thin ring (or "washer") of thickness dR and height l. The interior compartment is approximated as a hemisphere of radius R. The compartment volumes and their contact area (for diffusion and exchange) are thus

$$V_I = \frac{2}{3}\pi R^3, \quad V_E = 2\pi Rl \cdot dR, \quad A_{contact} = 2\pi Rl$$

Diffusion between compartments takes place through the surface that separates these, approximated as a cylinder of radius R and height l and area $A_{contact}$.

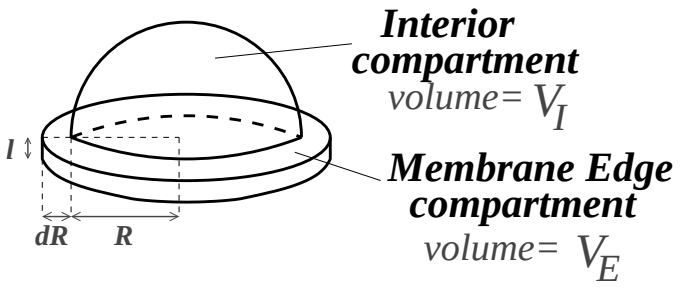

Figure S3: Cell geometry used in the two-compartment model (magnified view of the inset in Fig. 1).

Diffusion Flux Between Compartments

Because compartments are of vastly different sizes, our balance equations contain compartment volume factors to preserve mass conservation. We assume that the cofilin flux between compartments is diffusive, and thus proportional to concentration gradients. Taking into account the distinct volume of the compartments and the area through which diffusive flux takes place, we can write

$$\frac{d(V_E C_i^E)}{dt} = \omega\, D(C_i^I - C_i^E) \pm \text{reaction terms}, \tag{S20}$$

$$\frac{d(V_I C_i^I)}{dt} = -\omega\, D(C_i^I - C_i^E) \pm \text{reaction terms}, \tag{S21}$$

where D is the diffusion coefficient for cofilin (estimated as 10 μm^2/s (3)), and $\omega = 2\pi l$ with l, the thickness of the membrane edge compartment.

The factor ω is obtained as follows. Consider the geometry as in Fig. S3, and suppose C^E, C^I are concentrations of a given cofilin form in the edge and interior compartments. The diffusive flux from the edge to the interior is $J_D = \dfrac{D}{\lambda}(C^I - C^E)$, (number of molecules per unit time per unit area). λ is a typical length scale over which diffusion takes place, assumed to be the cell radius ($\lambda = R + dR \approx R$). The area of contact between the compartments is $A_{contact}$, so the number of molecules crossing this area per unit time is $A_{contact}\, J_D$. We define $\omega = 2\pi l$ and write

$$\frac{d}{dt}(V_E C^E) = (\omega R)\frac{D}{\lambda}(C^I - C^E) + \text{reaction terms} = D(2\pi l)(C^I - C^E) + ... \tag{S22}$$

The above equation is used to track forms of cofilin in the edge compartment that can diffuse between the two compartments. Similar terms occur in several equations in the model displayed below.

Equations for the Two-Compartment Model

PLC Activity

$$\frac{dPLC}{dt} = \bar{I}_{stim}(t) + I_{plc} - d_{plc}PLC\,, \tag{S23}$$

with the EGF stimulation profile

$$\bar{I}_{stim}(t) = \bar{I}_{stim0} \cdot [H(t - t_{on}) - H(t - t_{off})]\,, \tag{S24}$$

where $H(s)$ is the Heaviside function (i.e. unit step function that turns on at $t = 0$).

PIP_2 level

$$\frac{dP_2}{dt} = I_{p_2} - d_{p_2}P_2 - d_{hyd}\left(\frac{PLC - PLC_{rest}}{PLC_{rest}}\right)P_2\,. \tag{S25}$$

PIP_2-bound cofilin

$$\frac{dC_2}{dt} = k_{p_2}\left(\frac{P_2}{P_{2,rest}}\right)C_p^E - d_{c_2}C_2 - d_{hyd}\left(\frac{PLC - PLC_{rest}}{PLC_{rest}}\right)C_2\,. \tag{S26}$$

Active cofilin in the edge compartment

$$\begin{aligned}\frac{dC_a^E}{dt} &= d_{c2}C_2 + d_{hyd}\left(\frac{PLC - PLC_{rest}}{PLC_{rest}}\right)C_2 - k_{on}F\,C_a^E + k_{off}C_f \\ &\quad - k_{mp}C_a^E + k_{pm}C_p^E + \frac{\omega D}{V_E}(C_a^I - C_a^E)\,.\end{aligned} \tag{S27}$$

F-actin-bound cofilin in the edge compartment

$$\frac{dC_f}{dt} = k_{on}F\,C_a^E - k_{off}C_f - F_{sev}(C_f)\,, \tag{S28}$$

with the severing function

$$F_{sev}(C_f) = k_{sev}\,C_{f,rest}\left(\frac{C_f}{C_{f,rest}}\right)^n\,. \tag{S29}$$

G-actin-bound cofilin in the edge compartment

$$\frac{dC_m^E}{dt} = F_{sev}(C_f) - k_{mp}C_m^E + k_{pm}C_p^E + \frac{\omega D}{V_E}(C_m^I - C_m^E)\,. \tag{S30}$$

Phosphorylated cofilin in the edge compartment

$$\frac{dC_p^E}{dt} = k_{mp}(C_a^E + C_m^E) - 2k_{pm}C_p^E - k_{p_2}\left(\frac{P_2}{P_{2,rest}}\right)C_p^E + \frac{\omega D}{V_E}(C_p^I - C_p^E)\,. \tag{S31}$$

Active cofilin in the interior compartment

$$\frac{dC_a^I}{dt} = -k_{mp}C_a^I + k_{pm}C_p^I - \frac{\omega D}{V_I}(C_a^I - C_a^E)\,. \tag{S32}$$

G-actin-bound cofilin in the interior compartment

$$\frac{dC_m^I}{dt} = -k_{mp}C_m^I + k_{pm}C_p^I - \frac{\omega D}{V_I}(C_m^I - C_m^E)\,. \tag{S33}$$

Phosphorylated cofilin in the interior compartment

$$\frac{dC_p^I}{dt} = k_{mp}(C_a^E + C_m^E) - 2k_{pm}C_p^E - \frac{\omega D}{V_I}(C_p^I - C_p^E)\,. \tag{S34}$$

$$\tag{S35}$$

Barbed end production

$$\frac{dB}{dt} = \bar{A}F_{sev}(C_F) - k_{cap}B\,. \tag{S36}$$

Parameters are defined in Table 1 of the main text.

4 Determination of Parameter Values

Parameter Determination from Steady State Constraints

Several rate constants are obtained by imposing the steady state constraints (given in Eqn. (6)). Setting the left hand sides of Eqn. (7-17) to zero, the rate can be obtained by solving a nonlinear system of algebraic equations. We list the formulae obtained in Table S2. Note, however, that although algebraic expressions can be found, some of the rate constants also depend on the steady-state level of various cofilin forms. In many cases, no closed form expressions are possible, and parameters have to be found numerically. We list the steady-state values in Table S3.

Table S2: Parameter values for the two-pool model obtained by setting the steady-state fractions equal to R_i as given in Eqn. (10).

Parameter	Definition	Formula	Value
k_{p2}	binding rate C_p to PIP_2	$d_{c2}\dfrac{R2}{c^E_{p,ss}\cdot v_E}$	0.112/s
k_{pm}	dephosphorylation rate	$\dfrac{k_{mp}(Ra+Rm)-d_{c2}R_2}{2R_p}$	0.03/s
k_{sev}	severing rate	$\dfrac{k_{mp}R_m - k_{pm}R_p}{R_f}$	0.0012/s
$k_{on}F$	rate binding to F-actin	$\dfrac{R_f}{c^E_{a,ss}\cdot v_E}(k_{off}+k_{sev})$	0.198/s

Table S3: The steady-state concentrations for cofilin forms in the two-compartment model.

Edge Concentration	Value	Interior Concentration	Value
$c^E_{m,ss}$	0.036	$c^I_{m,ss}$	0.033
$c^E_{a,ss}$	0.068	$c^I_{a,ss}$	0.035
$c^E_{p,ss}$	0.165	$c^I_{p,ss}$	0.202
$c_{2,ss}$	12.4		
$c_{f,ss}$	2.19		

Parameter Fitting Procedure

Parameter fitting was done by solving constrained least-square problems utilizing the MATLAB fmincon function. Six parameters in total were fitted, and the remaining parameters were obtained either directly from the literature or from steady-state constraints. Data-fitting was done in two steps. First, parameters involving PLC dynamics (d_{plc} and I_{stim0}) were determined by fitting the solution of Eqn. (7), to the data from Mouneimne et al. (2) (see Fig. 2). We then fit the steady-state fractions R_2 and R_a, and the rate constants d_{hyd} and k_{mp}. Here, the full system (Eqn. (7-17)) was solved at each data-fitting iteration. Two separate data sets were used: (a) the barbed-end measurement reported

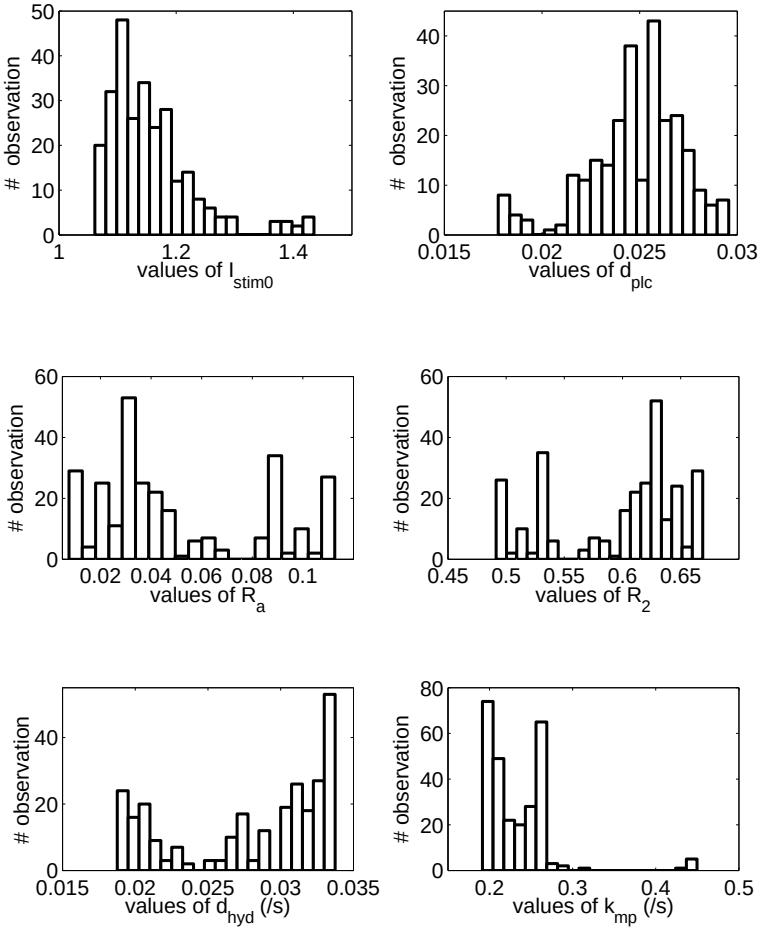

Figure S4: Distribution of parameter values obtained from the bootstrap procedure with 300 data sets. From the PLC data, the distributions for the parameters I_{stim0} and d_{plc} show strongly preferred values. However, the distributions for the remaining parameters are not as sharply peaked. This could be caused by the fact that there are only a small number of data points available for fitting. Nonetheless, simulations done with a set parameter with values that lie within the 95% interval (Table 1 in the paper) yield a result that is qualitatively similar.

in Mouneimne et al. (2) (denoted as (t_i, dat_b^i) with $i = 1, 2, 3$) and (b) the phospho-cofilin level shown in Song et al. (4) ((t_j, dat_{cp}^j), $j = 1, ..., 5$). Note that only the first three time points (first minute following stimulation) of the barbed end data were used as later barbed end level depends on Arp2/3 activity (not currently in our model). We define the sum squared-difference function,

$$G(R_2, R_a, d_{hyd}, k_{mp}) = \sum_{i=1}^{3} (b(t_i) - dat_b^i)^2 + \sum_{j=1}^{5} (c_p(t_j) - dat_{cp}^j)^2, \tag{S37}$$

where $b(t_i)$ is the ODE solution of the barbed end equation at time t_i with the specified parameter input, and $c_p(t_j) = v_E \cdot c_p^E(t_j) + v_I \cdot c_p^I(t_j)$, the whole-cell amount of phosphorylated cofilin at time t_j. This function was then used as an objective function to be minimized. The parameter values were also constrained such that $0 < R_2 < 0.7$, $0 < R_a < 0.1$ and the rate constants d_{hyd} and k_{mp} are positive.

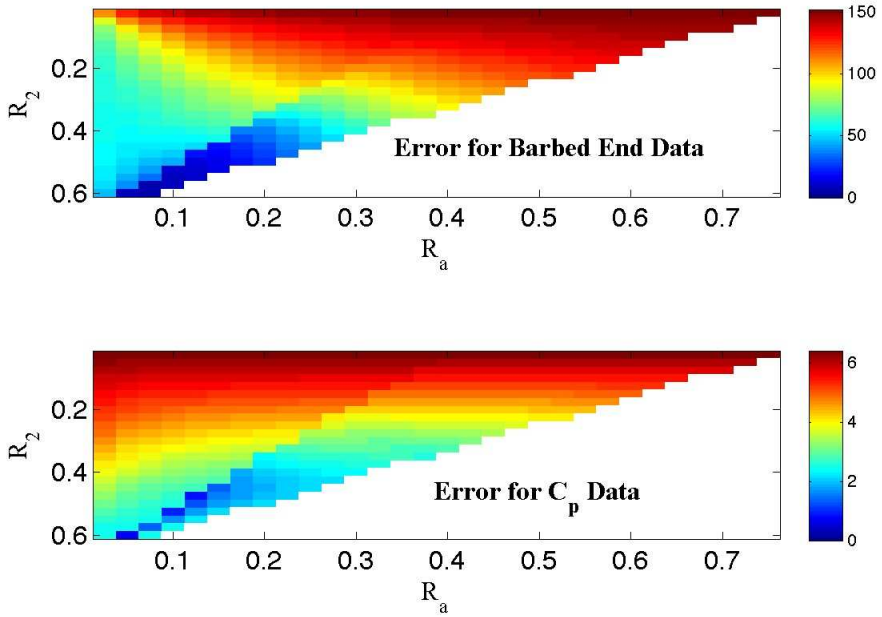

Figure S5: A good fit to barbed end (top panel) and phospho-cofilin (bottom panel) data sets is obtained only if the resting cell has a high level of PIP_2-bound cofilin, i.e. if $R_2 = v_E c_{2,SS}$ is large. Plots of error obtained from fitting d_{hyd} and k_{mp} while varying R_2 and $R_a = v_E c_a^E + v_I c_a^I$. The mean squared differences of simulation and experimental data are shown. Optimal parameters are in dark blue. (The white portion of the panels is inadmissible by conservation).

To measure the quality of data-fitting, a bootstrapping procedure was performed. 300 data sets were generated by sampling with replacement in the original data set. Parameter

fitting was done for each of these data-sets to obtain a distribution of parameter estimates. The 95% confidence intervals computed from the parameter distribution are listed in Table 1 of the article. Histograms indicating parameter distributions are shown in Fig. S4.

Sensitivity to Parameter Values

To ensure that our chosen parameter set is at a global minimum, we looked at the error in the data fits over a broad range of parameter values. Specifically, we performed multiple rounds of data-fitting by varying the steady state fractions R_2 and R_a and fit the rates k_{mp} and d_{hyd} for each (R_2, R_a) pair. The results are shown in Fig. S5. A good fit to both the amplification and the timing of the barbed end peak is obtained only for a large value of R_2 (approximately 50-60%). Values of R_2 and R_a are constrained more strictly by the phospho-cofilin data. There is a narrow range of values of R_2 and R_a that yields a good fit to the data. The final choice of parameter values listed in Table 1 (main paper) lies within the range that yields the minimal difference between simulation result and experimental observation.

5 Comparing the One and Two- Compartment Models

One-Pool Model Equations in Nondimensional Form

$$\frac{dplc}{dt} = d_{plc}(I_{stim}(t) + 1 - plc), \tag{S38}$$

$$\frac{dp_2}{dt} = d_{p_2}(1 - p_2) - d_{hyd}(plc - 1)p_2, \tag{S39}$$

$$\frac{dc_2}{dt} = k'_{p_2}\, p_2 c_p - d_{c_2} c_2 - d_{hyd}(plc - 1)c_2, \tag{S40}$$

$$\frac{dc_a}{dt} = d_{c_2} c_2 + k_{off} c_f - (k'_{on} F)c_a - k_{mp} c_a + k_{pm} c_p + d_{hyd}(plc - 1)c_2, \tag{S41}$$

$$\frac{dc_f}{dt} = (k'_{on} F)c_a - k_{off}\, c_f - k_{sev}\phi_F \left(\frac{c_f}{\phi_F}\right)^n, \tag{S42}$$

$$\frac{dc_m}{dt} = k_{sev}\phi_F \left(\frac{c_f}{\phi_F}\right)^n - k_{mp} c_m + k_{pm} c_p, \tag{S43}$$

$$\frac{dc_p}{dt} = k_{mp}(c_a + c_m) - 2k_{pm} c_p - k'_{p_2}\, p_2 c_p, \tag{S44}$$

$$\frac{db}{dt} = k_{cap}(1 - b) + A\, k_{sev}\phi_F \left(\frac{c_f}{\phi_F}\right)^n. \tag{S45}$$

Note that in this scaled version, each c_i represents a fraction of the total cofilin and $c_2 + c_a + c_f + c_m + c_p = 1$.

To make a correspondence between the models, note that the variables that are restricted to the cell edge in the two-compartment model are assumed to be uniformly distributed in the one-compartment model. This means that certain dilution factors are required to reflect the change of volume in which the reaction is assumed to occur. For example, in

the two-pool model, p_2, is the (non-dimensional) concentration of PIP_2 within the membrane edge compartment. In the one-pool model its (comparatively diluted) level would be $(p_2\, V_E)/V_{tot} = p_2 \cdot v_E$ in the reaction term describing cofilin rebinding to PIP_2 as now the reaction takes place in a larger single-pool. We absorb the volumetric factor in the one-pool rate constants by defining $k'_{p2} = k_{p2}\, v_E$. Similarly, for the term describing F-actin binding, we defined $k'_{on} = k_{on} v_E$.

Table S4: List of parameter values used for the one compartment model. Parameter fitting results and parameter values taken from the literature were used as in the two-compartment model. Parameter values shown in **bold** are used to maintain the same steady-state constraints.

Parameters	Definition	Values
EGF Stimulation		
I_0	Stimulus amplitude	1.14
t_{on}	Time at which EGF stimulus starts	25 s
t_{off}	Time at which EGF stimulus ends	85 s
PLC and PIP_2 Dynamics		
d_{plc}	Basal PLC degradation rate	0.026/s
d_{hyd}	PLC-induced PIP_2 hydrolysis rate	0.032/s
d_{p2}	Basal PIP_2 hydrolysis rate	0.002/s
Steady State Fractions of Cofilin		
R_2	Fraction bound to PIP_2	0.62
R_a	Fraction of free active form	0.04
R_p	Fraction phosphorylated/inactive	0.20
R_f	Fraction bound to F-actin	0.11
R_m	Fraction bound to G-actin	0.03
Cofilin Transition Rates		
d_{c2}	Basal c_2 hydrolysis rate	0.002/s
k_{off}	Unbinding rate from F-actin	0.005/s
$k_{on} F \cdot v_E$	Binding rate to F-actin	**0.02**/s
k_{mp}	Phosphorylation rate	0.186/s
k_{pm}	Dephosphorylation rate	0.03/s
$k_{p2} \cdot v_E$	Binding rate to PIP_2	**0.0047**/s
k_{sev}	Severing rate per cofilin molecule	**0.0012**/s
n	Degree of cooperativity in severing	4
Barbed End		
k_{cap}	Barbed end capping rate	1/s
A	Scaling factor for barbed end generation	**7735**

Comparison of Results: Effects of Localization

We compared the two-compartment model presented in the paper with the one compartment model that lacks the distinction between cell edge and interior. An important outcome of this comparison is the significance of localization (Fig. S6). Using similar parameters in both models, we find that the one-compartment variant significantly underestimates the barbed end peak, and the time course of its rising phase. One reason for this discrepancy is

that in the single compartment model, cofilin released from PIP_2 is quickly phosphorylated, leaving little to bind F-actin (k_{mp} is $\sim$2 orders of magnitude higher than $k_{on}F$). Even if the value of k_{mp} is adjusted in the single-compartment model so that the barbed end amplification is consistent with data (Fig. S7), the timing of the peak is too fast and the rise of phospho-cofilin much too slow relative to data (4). From these results, we conclude that membrane-edge localization of F-actin available for severing is an important factor in the large barbed end amplification in the presence of ongoing cofilin phosphorylation.

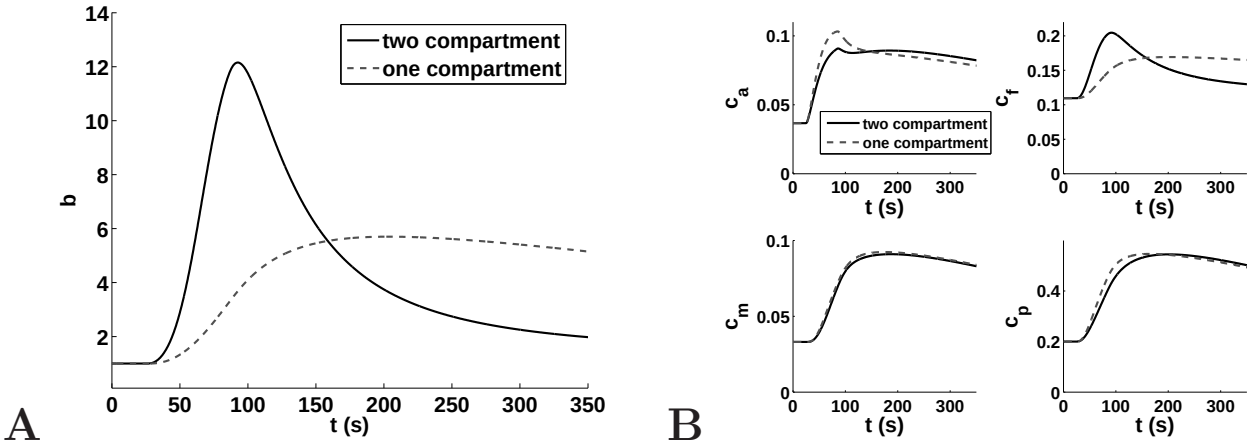

Figure S6: Effect of localization: a comparison of results obtained from the two-compartment model versus one-compartment model. Simulations of (A) barbed ends and (B) cofilin fractions (parameters as in Table 1 in the main paper). Experimental data from Mouneimne et al. (2) and Song et al. (4) (small open dots connected by line segments, shown in red) are shown for comparison.

This localization effect can also be observed by varying size of the membrane edge compartment. In Fig. S8, we show the barbed end profile obtained when v_E is increased from 5% up to 50%. In the latter, the barbed end profile is similar to the one obtained from the one-compartment model. Having a narrow membrane edge compartment allows for targeted and rapid actin binding. As the size of this compartment is increased, the bulk of the released active cofilin is immediately phosphorylated and fewer actin binding/severing events are observed. This is due to the fact that $k'_{on}F = k_{on}F/v_E$ decreases when v_E increases.

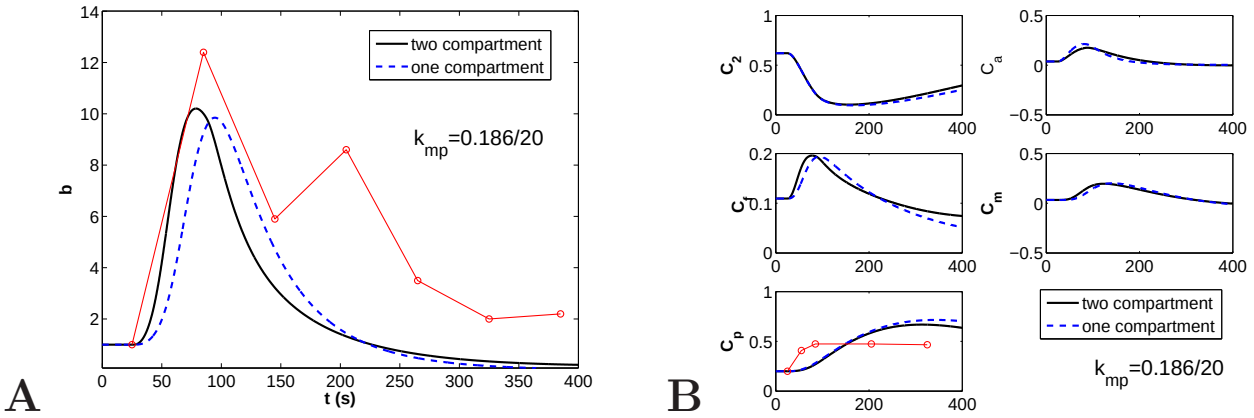

Figure S7: As in Fig. S6 but with a 20 times reduction in phosphorylation rate k_{mp}. (A) Barbed end level and (B) cofilin fractions and experimental data superimposed. In this case, large barbed end amplification is obtained for both models. However, the dynamics occur more rapidly in the two-compartment model than in the basic model. In turn, reducing the value of k_{mp} causes the rise of phosphorylated cofilin to be much too slow compared to observed experimental data.

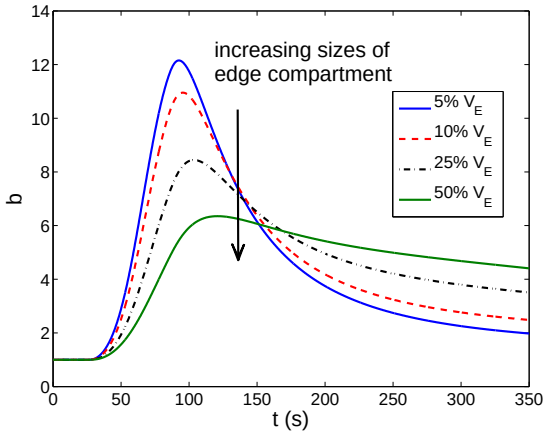

Figure S8: Barbed end profiles obtained from the two compartment model when the relative size of the membrane edge compartment is varied.

6 Results: Additional Figures

The following figures complement the discussion in the main article:

- Fig. S9 shows the dynamics of the nondimensionalized concentrations of cofilin forms in both the edge and interior compartments. Simulations are done under the basic set-up using the the two-compartment model (see Appendix and Table 1) with a 60 s EGF simulation applied at $t = 25$ s. For details, see Results: Basic Behavior section.

- Fig. S10 shows the dynamics of the cofilin fractions when LIMK/SSH is assumed to follow a dynamic increase in activity following simulation. For further description, see Results: Dynamics LIMK section.

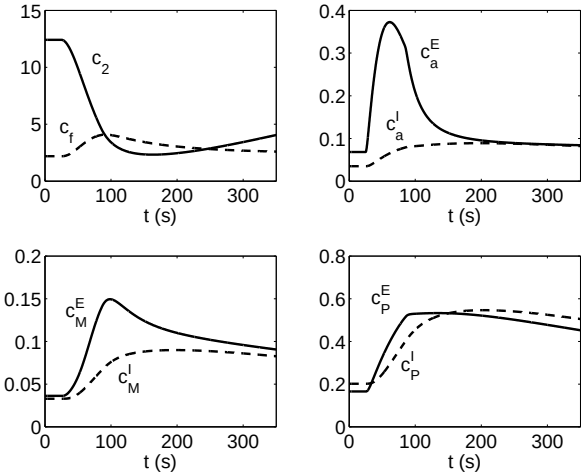

Figure S9: Nondimensional concentrations of cofilin forms (i.e. $c_i = C_i/C_{tot}$ for each i) in the edge and interior compartments. The values of c_2 and c_f are much higher than all other cofilin forms; both species are restricted to the small volume of the edge compartment.

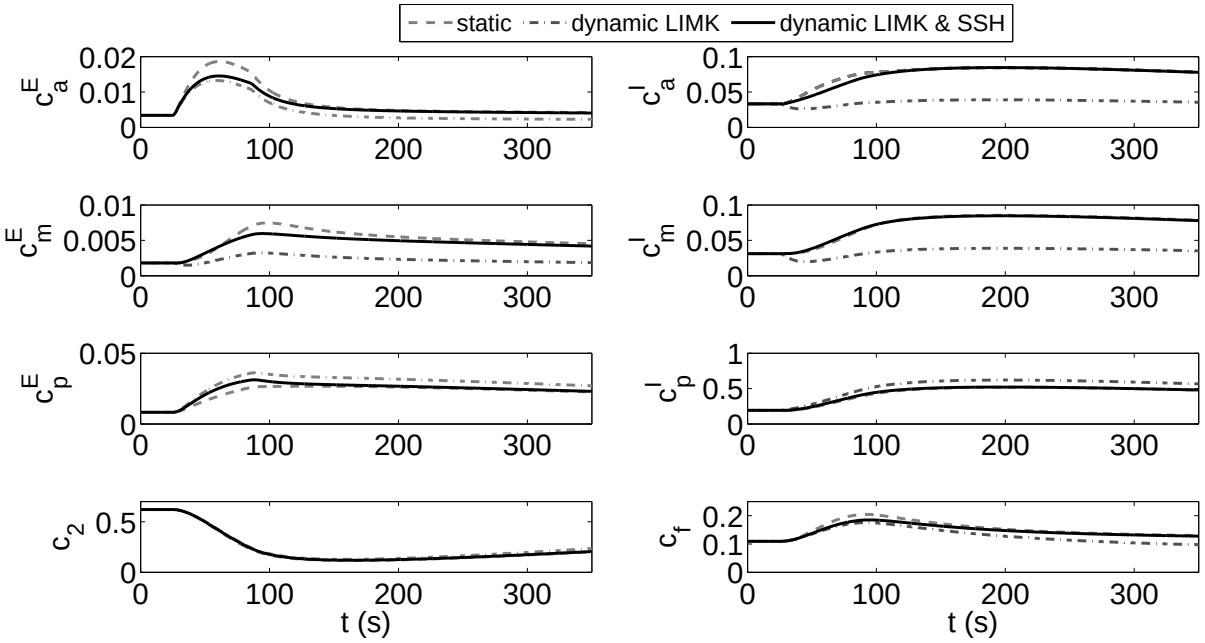

Figure S10: Dynamics of cofilin fractions for the time-varying LIMK and/or SSH.

References

[1] De La Cruz, E. M. 2005. Cofilin Binding to Muscle and Non-muscle Actin Filaments: Isoform-dependent Cooperative Interactions. *J Mol Biol*. 346:557 – 564.

[2] Mouneimne, G., L. Soon, V. DesMarais, M. Sidani, X. Song, S.-C. Yip, M. Ghosh, R. Eddy, J. M. Backer, and J. Condeelis. 2004. Phospholipase C and cofilin are required for carcinoma cell directionality in response to EGF stimulation. *J Cell Biol*. 166:697–708.

[3] Pollard, T. D., L. Blanchoin, and R. D. Mullins. 2000. Molecular mechanisms controlling actin filament dynamics in nonmuscle cells. *Annu Rev Biophys Biomol Struct*. 29:545–76.

[4] Song, X., X. Chen, H. Yamaguchi, G. Mouneimne, J. S. Condeelis, and R. J. Eddy. 2006. Initiation of cofilin activity in response to EGF is uncoupled from cofilin phosphorylation and dephosphorylation in carcinoma cells. *J Cell Sci*. 119:2871–81.